ACS APPLIED MATERIALS & INTERFACES

www.acsami.org Research Article

Accelerating the Phase Formation Kinetics of Alluaudite Sodium Iron Sulfate Cathodes via Ultrafast Thermal Shock

Yuhang Liu, Yujun Han, Zijing Song, Wanqing Song, Zhikai Miao, Yanan Chen,* Jia Ding,* and Wenbin Hu

Cite This: *ACS Appl. Mater. Interfaces* 2024, 16, 13828−13838 Read Online

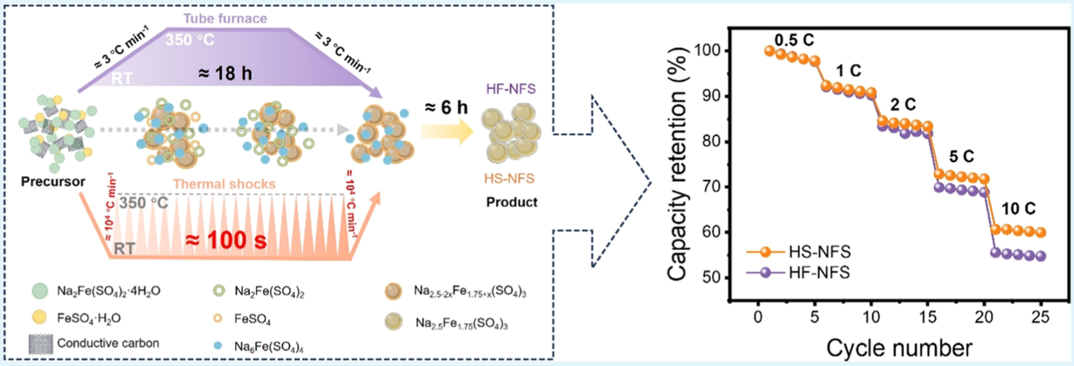

ABSTRACT: Alluaudite sodium iron sulfate (NFS) exhibits great potential for use in sodium-ion battery cathodes due to its elevated operating potential and abundant element reserves. However, conventional solid-state methods demonstrate a low heating/cooling rate and sluggish reaction kinetics, requiring a long thermal treatment to effectively fabricate NFS cathodes. Herein, we propose a thermal shock (TS) strategy to synthesize alluaudite sodium iron sulfate cathodes using either hydrous or anhydrous raw materials. The analysis of the phase formation process reveals that TS treatment can significantly facilitate the removal of crystal water and decomposition of the intermediate phase $Na_2Fe(SO_4)_2$ in the hydrous precursor. In the case of the anhydrous precursor, the kinetics of the combination reaction between Na_2SO_4 and $FeSO_4$ can be also accelerated by TS treatment. Consequently, pure NFS phase formation can be completed after a substantially shorter time of post-sintering, thereby saving significant time and energy. The TS-treated NFS cathode derived from hydrous precursor exhibits higher retention after 200 cycles at 1C and better rate capability than the counterpart prepared by conventional long-term tube furnace sintering, demonstrating the great potential of this novel strategy.

KEYWORDS: *thermal shock, alluaudite sodium iron sulfate, Na-ion batteries, cathode materials, rapid synthesis*

1. INTRODUCTION

The consumption of traditional fossil fuels inevitably results in an energy crisis and environmental contamination, requiring robust development of clean and renewable energy sources.[1−4] In recent years, electrochemical energy storage has become a crucial tool for establishing new energy systems and facilitating energy transformation.[5−7] Sodium-ion batteries (SIBs) exhibit similar energy storage mechanisms and enhanced safety compared to lithium-ion batteries.[8−11] Moreover, the costs of energy storage power stations will be substantially diminished owing to the exceedingly widespread sodium source on Earth.[12−14] However, developing cathode materials that possess comprehensive electrochemical performance poses a significant challenge in SIBs.[15−18]

Benefited from the stronger inductive effect and electronegativity of SO_4^{2-} than those of most polyanion groups,[19,20] alluaudite sodium iron sulfates (NFS) demonstrate the most elevated redox potential (3.8 V vs Na^+/Na) as compared to other polyanionic cathode candidates.[21] A three-dimensional (3D) framework with large Na^+ transfer tunnels along the *c*-axis is formed through the corner-sharing of edge-sharing Fe_2O_{10} groups and SO_4 tetrahedra. This structure exhibits stable long-term cycling and excellent rate performance.[22] Moreover, alluaudite sodium iron sulfate can be prepared by relatively low-temperature solid-state methods, which is favorable for large-scale production. There is also a vast possibility of efficient material recycling for NFS cathodes

Received: December 31, 2023
Revised: February 18, 2024
Accepted: February 23, 2024
Published: March 6, 2024

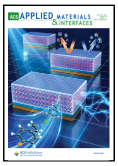

https://doi.org/10.1021/acsami.3c19618
ACS Appl. Mater. Interfaces 2024, 16, 13828−13838

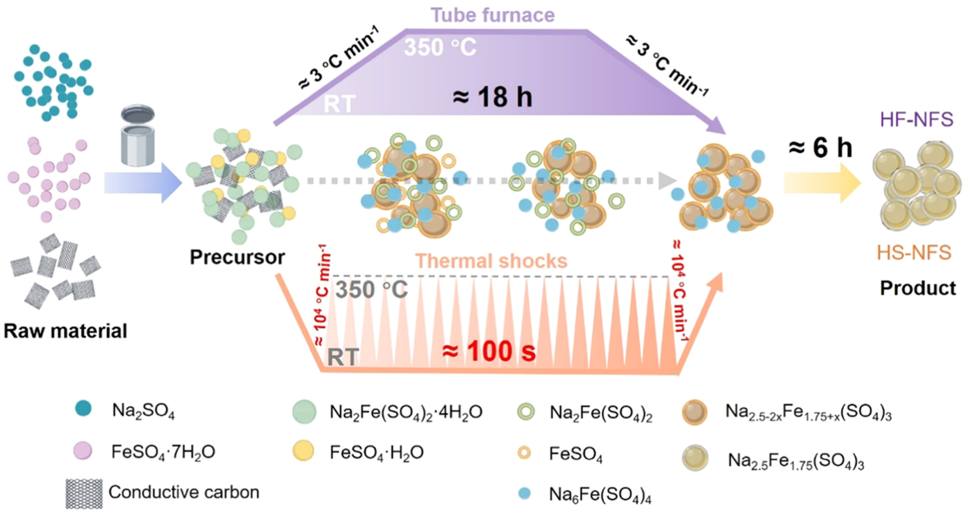

Figure 1. Schematic illustration of the synthesis processes of HS-NFS and HF-NFS samples.

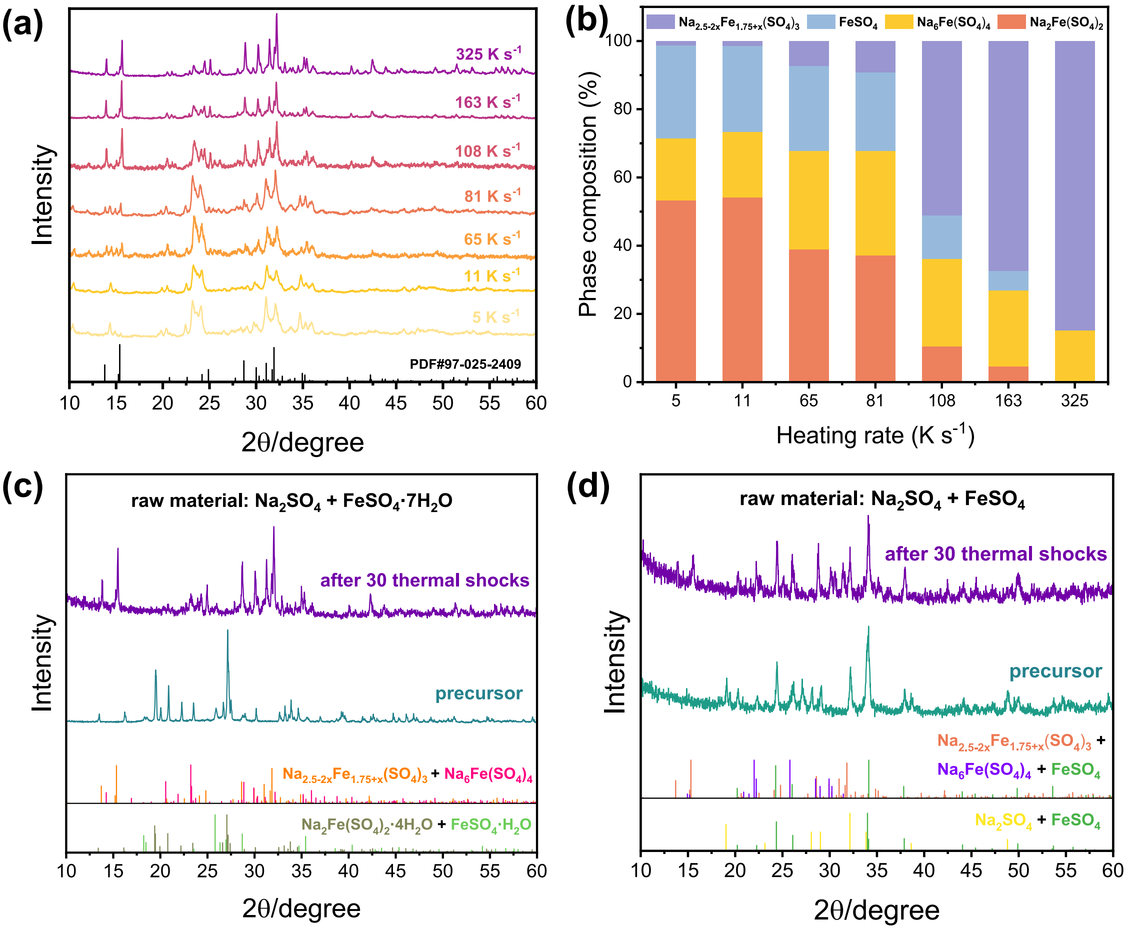

Figure 2. (a) XRD patterns of products from the hydrous precursors subjected to 30 thermal shocks at different heating rates. (b) Corresponding phase composition of the products derived from (a). XRD patterns of (c) hydrous precursor and (d) anhydrous precursor and the corresponding TS-treated products at a heating rate of 325 K s^{-1}.

because the Na−Fe−S chemical composition is nontoxic and environmentally friendly.[23]

The thermodynamic aspects of alluaudite sodium iron sulfate synthesis have been widely studied. Since $FeSO_4$ impurities were observed in $Na_2Fe_2(SO_4)_3$ by Yamada et al., they comprehensively studied the phase equilibrium of the Na_2SO_4−$FeSO_4$ system and concluded that excess sodium is needed to improve phase purity and obtain off-stoichiometric $Na_{2+2x}Fe_{2-x}(SO_4)_3$.[24] They found that the obtained product had the lowest weight fraction of the impurity phases when the value of x was 0.25. Consistent with this discovery, Ahuja et al. theoretically illustrated the inevitable precipitation of either $Na_6Fe(SO_4)_4$ or $FeSO_4$ impurities due to the duality of the phase boundaries by constructing chemical potential diagrams for each element.[25] Therefore, the purity of the final product is closely related to its specific chemical composition. Excessively low or high Na/Fe ratios lead to the generation of $FeSO_4$ and $Na_6Fe(SO_4)_4$, respectively. In addition, the effect of crystal water on the specific phase formation process has not yet been systematically investigated. Currently, the sintering time required in most solid-state methods is nearly up to 24 h,[14,16,20−23] which dramatically increases energy consumption and production cost. If it involves the process of dehydrating $FeSO_4·7H_2O$, the synthesis time will be even longer.[23,28−31] Therefore, there is an urgent need to develop an approach that can significantly reduce the duration of a solid-state sintering treatment, which can further augment the economic benefits of iron-based sulfates.

In this work, we present a thermal shock (TS) treatment strategy to prepare alluaudite sodium iron sulfate cathodes in the ultrashort period (≈100 s). The products obtained upon repeated TS treatment consist of an off-stoichiometric phase with trace amounts of $Na_6Fe(SO_4)_4$ residue. Therefore, a short sintering duration is sufficient to eliminate impurities and obtain a stoichiometric target phase after TS treatment. Furthermore, two types of precursors were investigated to analyze the influence of crystal water on phase formation by employing $FeSO_4·7H_2O$ or $FeSO_4$ as iron sources. Anhydrous $FeSO_4$ can be rapidly obtained by dehydrating $FeSO_4·7H_2O$ by the TS treatment. The results of X-ray diffraction (XRD) during TS-treating hydrous precursors indicate that thermal shock can rapidly remove crystal water in the precursor and significantly facilitate the decomposition of the intermediate phase $Na_2Fe(SO_4)_2$. In addition, the kinetics of the combination reaction between Na_2SO_4 and $FeSO_4$ in an anhydrous precursor can also be accelerated by this strategy. Compared to the conventional long-term sintering sample, the TS-treated cathode from the hydrous precursor possesses a smaller particle size and exhibits higher capacity retention after 200 cycles at 1C and better rate capability with a lower impedance and larger Na^+ diffusion coefficient.

2. RESULTS AND DISCUSSION

A schematic illustration of the synthesis process is exhibited in Figure 1. The detailed steps are provided in the Experimental section. The hydrous precursor was obtained by evenly mixing stoichiometric amounts of Na_2SO_4, $FeSO_4·7H_2O$, and conductive carbon via a ball-milling process. The resulting precursor was then loaded onto a conductive substrate in an Ar atmosphere. A notably rapid heating and cooling rate (10^4 °C min^{-1}) could be attained by applying a pulse current to the substrate, which is denoted as one thermal shock (TS). The conductive substrate will generate a rapid energy input in an instant and transfer heat to the materials on the substrate.[32,33]

The sintering temperature was set at 350 °C due to the susceptibility of sulfate to undergo decomposition at excessively high temperatures.[34] Following several thermal shocks, the collected powder was further pelletized and treated in a tube furnace at 350 °C for 6 h in an Ar flow. The final product prepared by this procedure from the hydrous precursor is denoted as HS-NFS. In order to investigate the influence of crystal water on phase formation, the product from the anhydrous precursor was also obtained by the same process (denoted as AS-NFS), where the predehydration of $FeSO_4·7H_2O$ was also realized by TS treatment. For comparison, the two previously mentioned precursors were pelletized and sintered in a tube furnace at 350 °C for 24 h in an Ar atmosphere without TS treatment and were denoted as HF-NFS and AF-NFS, respectively.

To assess the facilitating effect of thermal shock on the phase formation process, the phase compositions of the samples from hydrous precursors after an equivalent number of thermal shocks (30 times) at different heating rates were explored (as shown in Figure 2a). The target phase is $Na_{2.5}Fe_{1.75}(SO_4)_3$ (PDF#97−025−2409) when the Na/Fe ratio of the precursor is adopted as 1.5:1. When the heating rate of the thermal shock was set to 5 K s^{-1}, the corresponding products were mainly composed of $Na_2Fe(SO_4)_2$, $Na_{2.5-2x}Fe_{1.75+x}(SO_4)_3$, $Na_6Fe(SO_4)_4$, and $FeSO_4$ (Figure 2b). The first three phases originate from the dehydration and incomplete decomposition of $Na_2Fe(SO_4)_2·4H_2O$ in the precursor. $FeSO_4$ was generated by the removal of crystal water in $FeSO_4·H_2O$.

As the heating rate exceeded 11 K s^{-1}, there were scarcely any discernible alterations in the phase composition of the product. Of note, $Na_{2.5-2x}Fe_{1.75+x}(SO_4)_3$ can be obviously generated as the heating rate is further increased to 65 K s^{-1}. Although the relative content was low, this phenomenon indicates that thermal shock is capable of promoting phase formation of $Na_{2.5-2x}Fe_{1.75+x}(SO_4)_3$. Benefiting from this treatment, the content of the designated product gradually increased in proportion to the increase in the heating rate. Specifically, as long as the heating rate reaches 108 K s^{-1} or higher, the $Na_{2.5-2x}Fe_{1.75+x}(SO_4)_3$ phase constitutes the dominant component in the product. Furthermore, the proportion of the $Na_{2.5-2x}Fe_{1.75+x}(SO_4)_3$ phase was highest at an ultimate heating rate of 300 K s^{-1}. As shown in Figures S1 and S2, the thermogravimetric analysis combined with differential scanning calorimetry (TGA-DSC) was also conducted during heating of the hydrous precursor at heating rates of 3 and 100 °C min^{-1}. The TGA curves for both samples exhibited similar shapes under both slow- and fast-heating conditions. The difference is that the dehydration temperature shifted to a higher level due to the higher heating rate. Note that the accelerated heating could potentially result in a more pronounced baseline drift.[35] The focus was primarily on analyzing the peak shapes of the DSC curves rather than their absolute values. However, no extra endothermic or exothermic peaks were observed in either sample, except for the shift in the peak position, probably due to the change in reaction kinetics resulting from the rapid heating process. Consequently, the specific process of phase formation during sintering must be analyzed to determine why thermal shock can accelerate the reaction kinetics.

Crystal water significantly influences the phase formation of sodium iron sulfate.[22,23,26−31] Depending on whether the iron source ($FeSO_4·7H_2O$) in the ingredients is predehydrated, two types of precursors can be obtained during the high-energy ball-milling process. Apparently, the hydrous precursors obtained after ball milling are not simply mixtures of raw reagents. Na_2SO_4 can readily react with $FeSO_4·7H_2O$ to generate hydrated iron-based sodium sulfate.[36] The reaction occurring is depicted in eq 1

$$Na_2SO_4 + FeSO_4·7H_2O \rightarrow Na_2Fe(SO_4)_2·4H_2O + 3H_2O \quad (1)$$

Figure 2c shows that the hydrous precursor was mainly composed of $Na_2Fe(SO_4)_2·4H_2O$ and trace amounts of $FeSO_4·H_2O$.[37] After 30 thermal shocks were applied to the precursor, $Na_{2.5-2x}Fe_{1.75+x}(SO_4)_3$ could be successfully prepared, yet with the Na/Fe ratio slightly deviating from the stoichiometric ratio

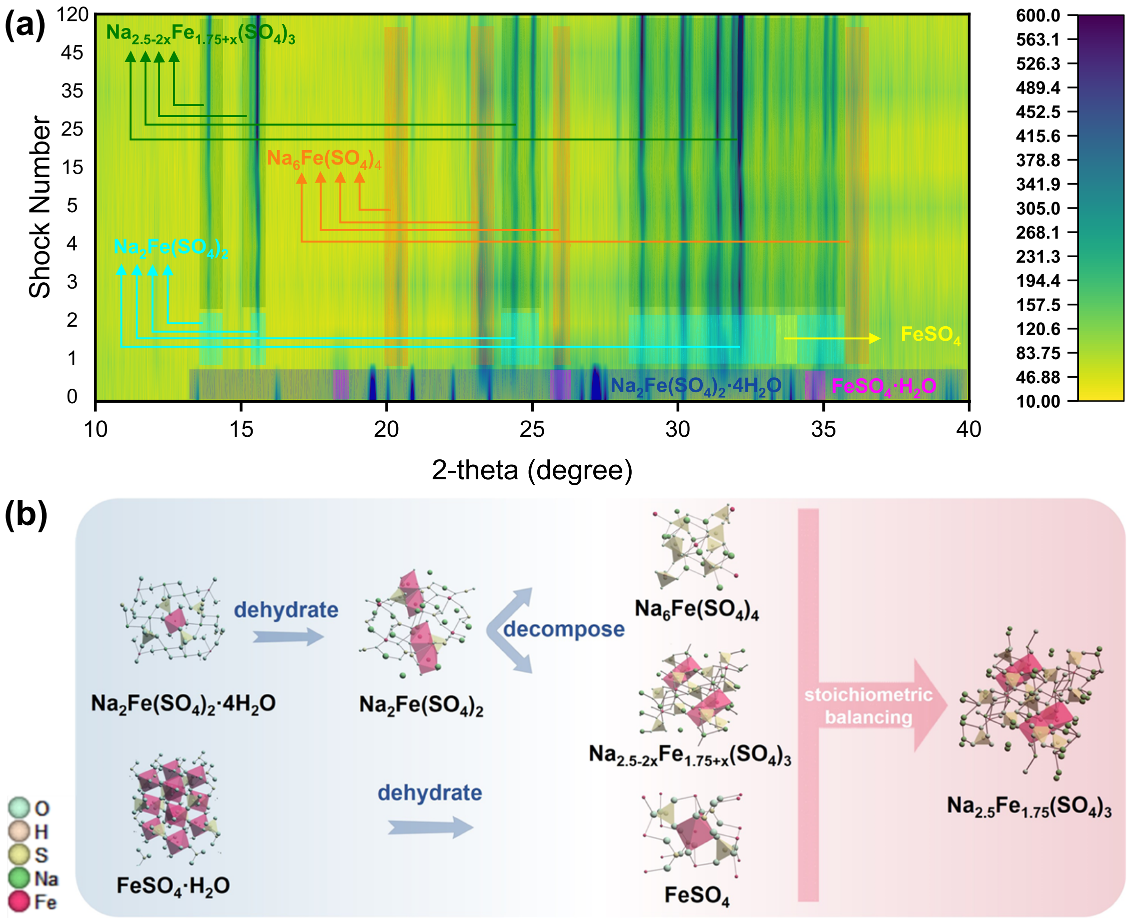

Figure 3. (a) Contour plots of the XRD patterns of the TS-treated products from hydrous precursor with a 1.5:1 Na/Fe ratio. The blue, purple, orange, cyan, yellow, and green squares indicate the peaks of $Na_2Fe(SO_4)_2·4H_2O$, $FeSO_4·H_2O$, $Na_6Fe(SO_4)_4$, $Na_2Fe(SO_4)_2$, $FeSO_4$, and $Na_{2.5-2x}Fe_{1.75+x}(SO_4)_3$, respectively. (b) Schematic of the phase transformation of the hydrous precursor upon sintering.

due to a trace amount of $Na_6Fe(SO_4)_4$. Unlike the hydrous precursor, Figure 2d indicates that the anhydrous precursor retained its initial composition after the ball-milling procedure, probably due to the absence of crystal water in the raw materials. A small amount of $Na_{2.5-2x}Fe_{1.75+x}(SO_4)_3$ and more $Na_6Fe(SO_4)_4$ phase were formed in the product, accompanied by the retention of $FeSO_4$ after the same number of thermal shocks. For comparison, the above two precursors were sintered through traditional thermal treatment utilizing a tube furnace. Figures S3 and S4 indicate that the pure phase can be successfully obtained after calcination for 24 h regardless of the presence of crystal water in the raw materials.

Rapid heating and cooling during thermal shock can result in significant energy fluctuations that are distinct from those of the traditional sintering process. Hence, it is essential to scrutinize the phase-forming behavior during thermal shocks. The hydrous and high Na/Fe ratio (≈1.5:1) precursor was first selected for investigation. Figure 3a shows contour plots of the XRD patterns of the TS-treated products from hydrous precursor with a 1.5:1 Na/Fe ratio. $Na_2Fe(SO_4)_2·4H_2O$ and $FeSO_4·H_2O$ were dehydrated rapidly after only one thermal shock, accompanied by slight decomposition to $Na_6Fe(SO_4)_4$ and $Na_{2.5-2x}Fe_{1.75+x}(SO_4)_3$ $(0 \leq x < 0.25)$.[38] The reaction for this process is depicted in eq 2

$$(8 + 8x)Na_2Fe(SO_4)_2 \rightarrow 4Na_{2.5-2x}Fe_{1.75+x}(SO_4)_3 + (1 + 4x)Na_6Fe(SO_4)_4 \tag{2}$$

As the number of thermal shocks gradually increased above 10, $Na_{2.5-2x}Fe_{1.75+x}(SO_4)_3$ was clearly observed in the product. The subsequent shock process revealed that the Na/Fe/S proportions of sodium-rich phase $Na_6Fe(SO_4)_4$, off-stoichiometric phase $Na_{2.5-2x}Fe_{1.75+x}(SO_4)_3$, and $FeSO_4$ phases gradually approached the anticipated target stoichiometric ratio of 2.5:1.75:3, as shown in Figure 3b. Thereafter, the impurity phases exhibited negligible change when the number of thermal shocks reached up to 120, indicating that the decomposition of $Na_2Fe(SO_4)_2$ was complete, but the process of balancing chemical composition of $Na_6Fe(SO_4)_4$, $Na_{2.5-2x}Fe_{1.75+x}(SO_4)_3$, and $FeSO_4$ was almost unable to further proceed during thermal shocks. Hence, though thermal shocks could significantly promote phase formation, it is necessary to sinter in a tube furnace for a short time to further increase the purity of the target product.

For alluaudite sodium iron sulfates, the probability of producing $FeSO_4$ impurities is higher when adopting a lower Na/Fe ratio.[24−26] Figure S5 describes this phenomenon during TS treatment. Compared to the 1.5:1 Na/Fe ratio precursor, the 1:1 Na/Fe ratio precursor exhibited a similar reaction path. Specifically, the removal of crystal water and the decomposition of $Na_2Fe(SO_4)_2$ were still accelerated by thermal

https://doi.org/10.1021/acsami.3c19618
ACS Appl. Mater. Interfaces 2024, 16, 13828−13838

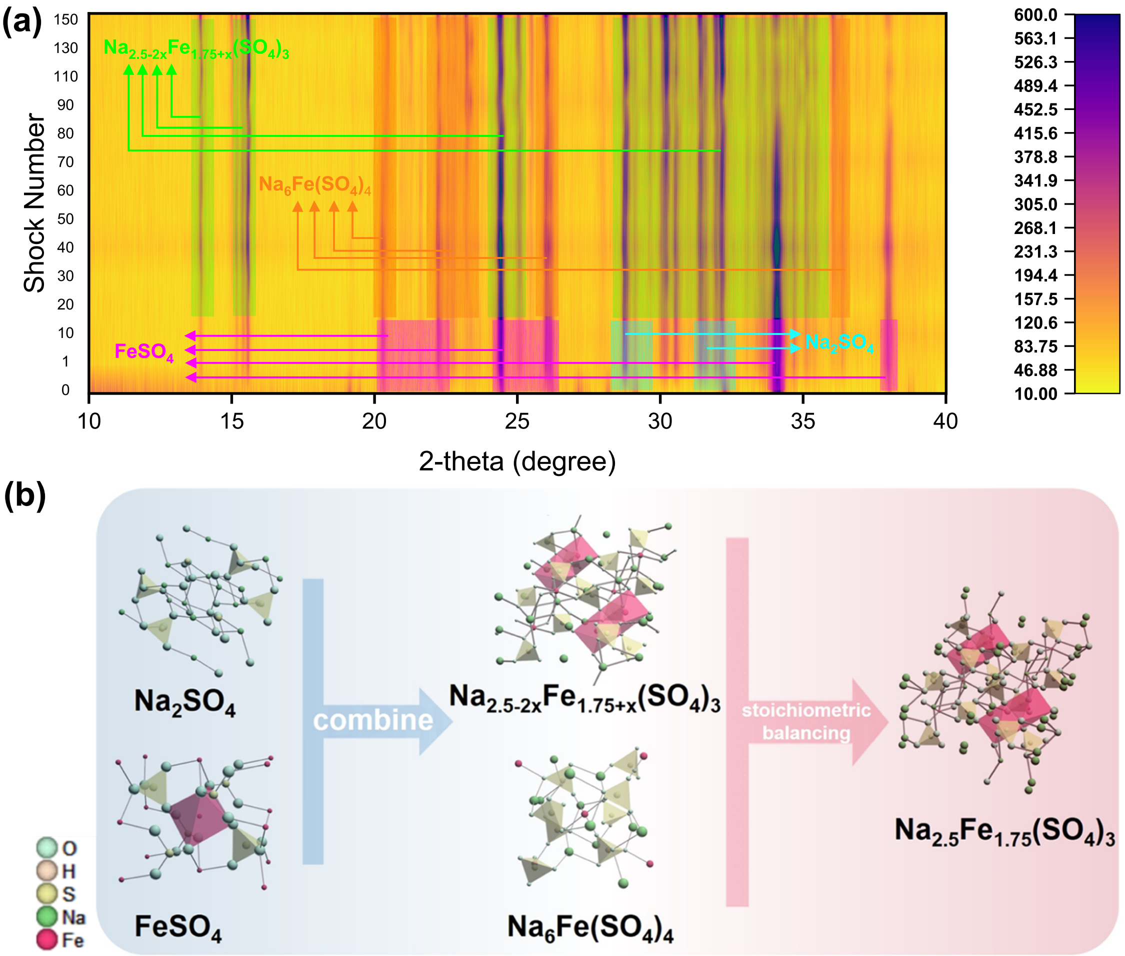

Figure 4. (a) Contour plots of the XRD patterns of the TS-treated products from anhydrous precursor with a 1.5:1 Na/Fe ratio. The purple, blue, orange, and green squares indicate the peaks of $FeSO_4$, Na_2SO_4, $Na_6Fe(SO_4)_4$, and $Na_{2.5-2x}Fe_{1.75+x}(SO_4)_3$, respectively. (b) Schematic of the phase transformation of the anhydrous precursor upon sintering.

shock. However, the subsequent process of balancing the chemical composition of the two decomposed products and $FeSO_4$ displayed persistently sluggish kinetics. The effect of this process was more pronounced at low Na/Fe ratios, owing to the relatively higher $FeSO_4{\cdot}H_2O$ content. Therefore, it required more thermal shocks or extended sintering to fully complete the reaction. Moreover, the diffraction peak of $FeSO_4$ was still observed even after 120 thermal shocks, indicating that the Na/Fe ratio indeed influenced the purity of the product.[21,24]

Based on the XRD characterization, we found that the decomposition of the intermediate phase was sensitive to violent energy fluctuations, leading to faster phase formation kinetics. The contour plots of the XRD patterns (Figure 4a) also reveal the phase-forming acceleration effect of the thermal shocks on the anhydrous precursor. At the beginning of the reaction, the reactants $FeSO_4$ and Na_2SO_4 underwent a combination reaction to form the off-stoichiometric phase $Na_{2.5-2x}Fe_{1.75+x}(SO_4)_3$ and the sodium-rich phase $Na_6Fe(SO_4)_4$. Both phases are generated almost simultaneously, resulting in a large deviation from the expected stoichiometric ratio of the target product. Subsequently, the Na/Fe/S composition between the two phases gradually approached the anticipated stoichiometric ratio of 2.5:1.75:3, as shown in Figure 4b. However, the consumption of the sodium-rich phase through this process was significantly slow, resulting in its apparent retention despite a substantial number of shocks (≈150). Compared to the hydrous precursor, as depicted in eq 2, the production of the sodium-rich phase $Na_6Fe(SO_4)_4$ is small due to its very high Na/Fe ratio. Therefore, the anhydrous precursor yields more $Na_6Fe(SO_4)_4$ impurities than the hydrous precursor after the same TS treatment, although the Na/Fe ratios are equal.

As mentioned earlier, violent energy fluctuations caused by thermal shocks could significantly promote phase formation kinetics. However, impurities such as $Na_6Fe(SO_4)_4$ or $FeSO_4$ were still retained due to the sluggish kinetics of the stoichiometric balancing process, and a short period of traditional tube furnace calcination was still needed to further eliminate the impurities. A pure phase of the target product HS-NFS was obtained after calcination of only 6 h. In order to acquire precise phase information, powder X-ray diffraction was used to identify the phase composition and atomic site occupancy. Rietveld refinement of the XRD data was conducted, and the results are presented in Figure 5a. All of the diffraction peaks were indexed to alluaudite sodium iron sulfate in the space group of monoclinic $C2/c$ symmetry[22] with lattice parameters a = 12.6586 Å, b = 12.7820 Å, c = 6.5256 Å, β = 115.546°, and V = 952.632 Å^3. Detailed structural data, including the atomic characteristics of HS-NFS, are provided in Table S1 in the Supporting Information. Apart from HS-NFS, AS-NFS is also refined, as shown in Figure S6. A

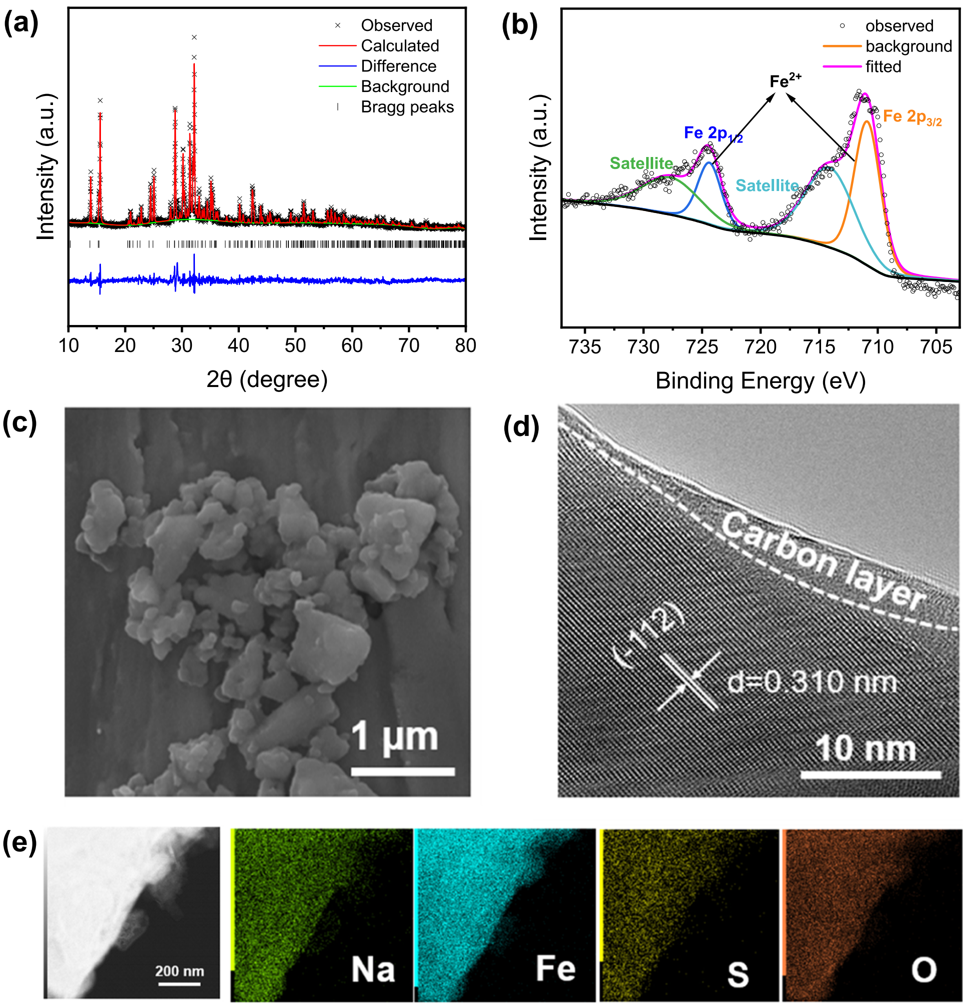

Figure 5. (a) XRD pattern of HS-NFS and Rietveld refinement. (b) Fe 2p core level XPS spectrum of the HS-NFS sample. (c) SEM and (d) TEM images of HS-NFS. (e) STEM-EDS mapping results exhibit the presence of the specified elements in the HS-NFS sample.

significant amount of $Na_6Fe(SO_4)_4$ remained after sintering for a duration of 6 h subsequent to TS treatment, demonstrating that the elimination of the impurity phase is challenging. The refinement results (Tables S2 and S3) indicated that the amount of sodium-rich impurity was ≈24.4 wt %, which would inevitably affect the electrochemical performance.

As iron-based materials are susceptible to oxidation, especially during the long-term sintering process,[34] XPS characterization was employed to probe the valence states of HS-NFS and HF-NFS. Figure 5b illustrates the high-resolution spectrum of Fe 2p, revealing two distinctive peaks at 711.1 and 724.6 eV, corresponding to Fe $2p_{3/2}$ and Fe $2p_{1/2}$ orbitals, respectively.[29,39] Apart from the two main peaks of Fe 2p, two corresponding satellite peaks at 714.2 and 727.9 eV were also observed.[40] After TS pretreatment, there was a notable decrease in the time required for sintering, resulting in no oxidation in HS-NFS. However, as shown in Figure S7, a weak Fe^{3+} peak was captured at 719.8 eV,[22] suggesting that HF-NFS inevitably underwent trace oxidation due to long-term sintering.

The morphology of HS-NFS was analyzed by using scanning electron microscopy (SEM) and transmission electron microscopy (TEM) (Figure 5c,d). The average particle size was around 200 to 500 nm. TEM reveals the apparent presence of lattice fringes, indicating excellent crystallinity of the sample. The lattice spacing of the (−112) crystal plane was 0.310 nm, which is in accordance with the peak at 28.68° in the XRD pattern.[37] Moreover, the thickness of the uniform wrapping carbon layer was measured to be ca. 3 nm, which could significantly promote the electronic conductivity of the material.[39,41−43] In addition, an energy dispersive spectrometer (EDS) with element mapping was employed to characterize the distribution of the elements (Figure 5e). It was observed that the elements Na, Fe, S, and O exhibited a homogeneous distribution within the particles with no significant sodium-rich areas. This finding effectively demonstrated a remarkably pure phase, as shown in Figure 5a. For comparison, HF-NFS was also characterized through SEM and TEM. As shown in Figure S8, significant aggregation of the superfine primary particles could be observed on the surface because of long-period sintering,[27,44,45] causing the average size of the secondary particles to be larger than that of HS-NFS, reaching ca. 2 μm. Additionally, Figure S9 indicates that HF-NFS appears to have less distinct lattice fringes than HS-NFS, which probably affects its structural stability.

Since the number of thermal shocks has a significant effect on the phase composition, samples with 120 thermal shocks were selected for electrochemical testing in coin cells featuring a sodium metal anode. The carbon contents of samples derived from hydrous and anhydrous precursors were, respectively,

https://doi.org/10.1021/acsami.3c19618

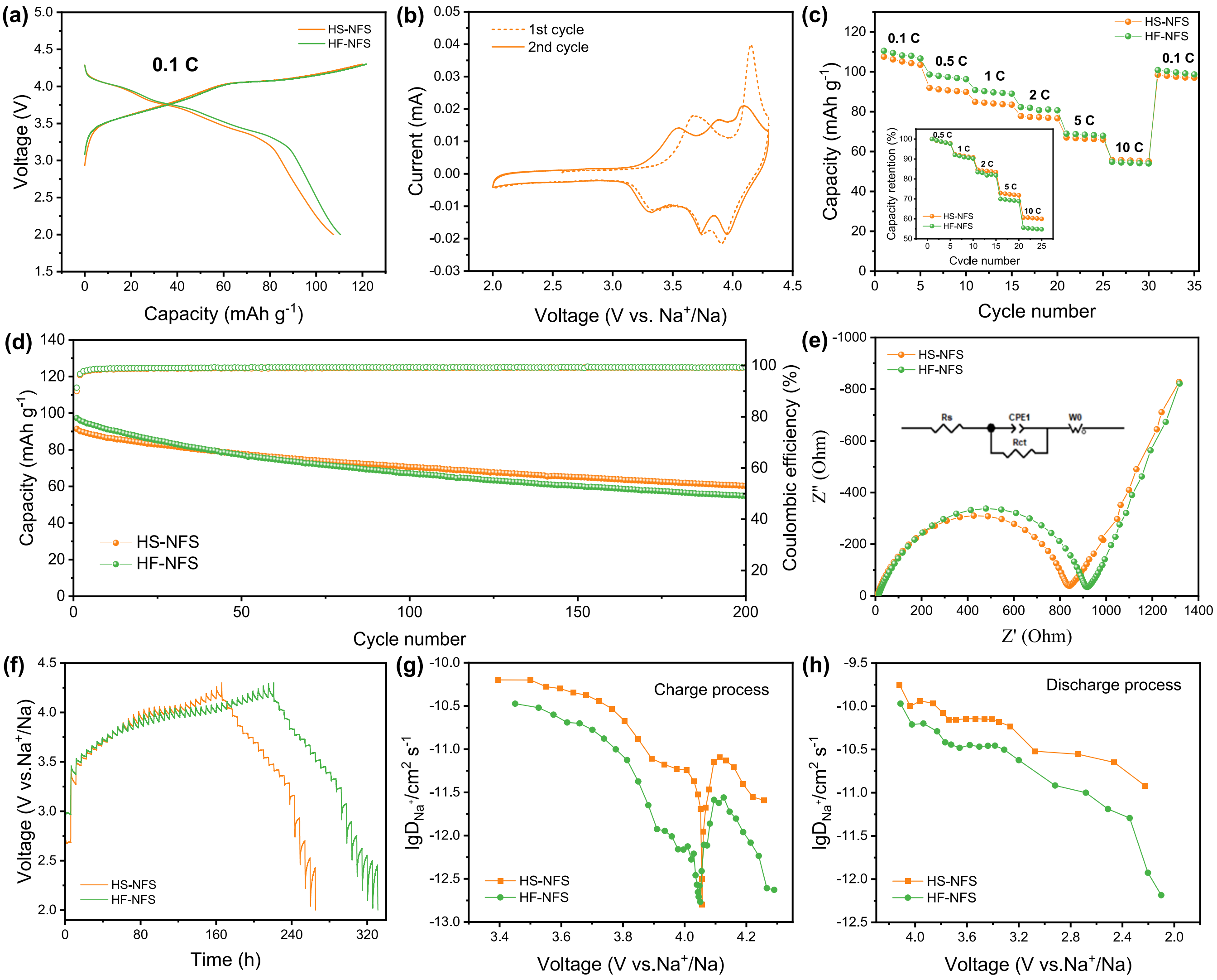

Figure 6. Electrochemical performances of HS-NFS and HS-NFS cathodes. (a) Galvanostatic charge−discharge curves. (b) Cyclic voltammetry (CV) curves of the HS-NFS electrode. (c) Rate capability. The inset shows the corresponding capacity retentions at different rates. (d) Cycling stability up to 200 cycles at 1C. (e) Electrochemical impedance spectra (EIS) of both electrodes. The inset shows the equivalent circuit used to interpret the EIS data. (f) Voltage profiles during GITT, and the diffusion coefficient of Na$^+$ as a function of voltage calculated from the GITT curve during the (g) charge and (h) discharge processes.

determined to be 2.70 and 1.88 wt % by an infrared absorption carbon−sulfur analyzer. The loading of the active material after slurry coating on the current collector was about 1.5 mg cm^{-2}. The coin cells were tested between 2.0 and 4.3 V, the current density was determined by the testing rate (1C = 120 mAh g^{-1}), and the theoretical specific capacity was determined based on the 1.75 electron transfer mechanism in the $Na_{2.5}Fe_{1.75}(SO_4)_3$ component.[37,41]

Figure 6a shows the initial galvanostatic charge−discharge curves of HS-NFS and HF-NFS at 0.1C. Both cathodes displayed almost identical voltage plateaus and curve shapes with comparable specific capacities of 107.6 and 110.5 mAh g^{-1}, respectively. It is vital to note that the initial charge−discharge curve of HS-NFS exhibited a discernible difference compared to that of the second cycle. This disparity can be better observed in the cyclic voltammetry (CV) curves (Figure 6b), while there are no evident distinctions between the initial and subsequent cycles. The sharp peak at 4.1 V during the initial charging process is probably attributed to the structural distortion derived from Fe migration into Na(1) sites. Since this transition is irreversible, the two oxidation peaks no longer appear in the second cycle and are replaced by three new peaks (at ∼3.48, ∼3.76, and ∼4.08 V), which are attributed to the extraction of Na$^+$ from the Na/Fe(1), Na(3), and Na(2) sites, respectively.[29,37,42,46−48] In comparison, a CV test was also employed to assess HF-NFS, as shown in Figure S10. Consistent with the GCD curves illustrated in Figure 6a, both electrodes demonstrated highly similar CV characteristics, but HF-NFS displayed a slightly higher peak current, potentially suggesting a higher charge/discharge capacity under a low current density. Despite this fact, the electrical resistivity of HS-NFS tested by the four-probe resistivity tester shows an electronic conductivity of 1.88 × 10^{-4} S cm^{-1} at a thickness of 0.78 mm under a pressure of 2.75 MPa, while HF-NFS shows a conductivity of 1.15 × 10^{-4} S cm^{-1} at a thickness of 0.63 mm under a pressure of 3.11 MPa, indicating that HS-NFS possesses potentially better rate capability. Besides, the rate performance shown in Figure 6c demonstrates that HS-NFS exhibited the same capacity at 10C as HF-NFS with a remarkably higher capacity retention of 60.7%, surpassing 55.6% that of HF-NFS (inset in Figure 6c).

To conduct a more comprehensive analysis of the electrochemical durability of the electrodes, their cycle performance was examined at 1C, as shown in Figure 6d. After 200 cycles, HS-NFS and HF-NFS exhibited capacity retentions of 65.9 and 56.3%, respectively, indicating the better cycling stability of HS-NFS. In addition, a smaller charge transfer impedance (R_{ct}) was observed in HS-NFS than in HF-NFS, as evidenced by the EIS measurements in Figure 6e, suggesting an improvement in the electrons/ions transportation within the HS-NFS electrode, thereby displaying better cycling stability.[42]

The galvanostatic intermittent titration technique (GITT) was performed to further estimate Na^+ migration kinetics (Figure 6f). It can be seen that the voltage drop of HF-NFS during relaxation was more obvious than that of HS-NFS, resulting in a longer charge process though its discharge capacity is slightly higher. The diffusion coefficients of Na^+ ions at different voltage states were also calculated and are displayed in Figure 6g,h.[49] Specifically, the D_{Na+} of HS-NFS was higher than that of HF-NFS, potentially indicating a higher capacity retention of HS-NFS at a high rate. A decrease of the diffusion coefficient at 4.05 V was observed in both samples, which is attributed to the fact that Na^+ is almost completely extracted from the Na(3) site in this charged state and the migration of Fe from the Fe(1) to the Na(1) site hinders further diffusion of Na^+ from the Na(2) site.

Apart from considering the difference in sintering treatment during the synthesis processes, the impact of crystal water in the precursors also cannot be ignored; thus, electrochemical characterization of AS-NFS and AF-NFS from the anhydrous precursors was conducted. As mentioned above, the sodium-rich impurity $Na_6Fe(SO_4)_4$ was not entirely eliminated during the brief sintering period due to the sluggish kinetics of the stoichiometric balancing process. Moreover, the electrochemical properties of $Na_6Fe(SO_4)_4$ are undesirable,[23,44] causing AS-NFS to exhibit a lower specific capacity (≈98.8 mAh g^{-1}) compared to AF-NFS (≈115.4 mAh g^{-1}), as shown in Figure S11. Nonetheless, it is noteworthy to mention that in comparison to the samples from the hydrous precursor, both AS-NFS and AF-NFS demonstrated significantly higher capacity retentions of 72.9 and 71.4% at 10C (Figure S12), indicating faster ionic-transfer kinetics and more reversible active Na^+ sites.[26,38] Moreover, the results from the long-cycling examination of both electrodes from the anhydrous precursor depicted in Figure S13 further substantiated the elevated capacity preservation after 200 cycles, with 87.2 and 88.4%, respectively, showing better structural stability.

Based on the above discussion, both AS-NFS and AF-NFS delivered distinctly better electrochemical performance. This may be ascribed to the different reaction paths and kinetics, leading to differences in the fine structure and crystallinity of the final product, which affects the number of effective activated Na^+ sites that can participate in the electrochemical reaction as well as the stability of the crystal structure.[50,51]

3. CONCLUSIONS

In summary, a thermal shock (TS) fabrication strategy was proposed to prepare alluaudite sodium iron sulfate cathodes with or without prior dehydration of $FeSO_4{\cdot}7H_2O$, which significantly reduced the sintering time compared to the conventional solid-state method. Taking the Na/Fe ratio of 1.5:1 as an example, the phase formation process during TS-treating hydrous precursor consists of the removal of crystal water in the precursor, the decomposition of the intermediate phase $Na_2Fe(SO_4)_2$, and the stoichiometric balancing process between $Na_{2.5-2x}Fe_{1.75+x}(SO_4)_3$, $Na_6Fe(SO_4)_4$, and $FeSO_4$. In the case of the anhydrous precursor, it was a combination reaction between the reactants Na_2SO_4 and $FeSO_4$ to form $Na_{2.5-2x}Fe_{1.75+x}(SO_4)_3$ and $Na_6Fe(SO_4)_4$, after which the two phases underwent stoichiometric balancing to form the final product $Na_{2.5}Fe_{1.75}(SO_4)_3$. The analysis of the phase formation process reveals that TS can significantly accelerate the kinetics of dehydration, decomposition, and combination reactions. The as-prepared HS-NFS possesses a smaller particle size and exhibits potentially better electrochemical properties than long-term sintered samples with lower impedance and larger Na^+ diffusion coefficients. The AS-NFS cathode was found to have significantly better rate performance and cycling stability. This work elucidates rational solutions for further optimizing the synthesis of alluaudite sodium iron sulfate cathodes.

4. EXPERIMENTAL SECTION

4.1. Materials. Iron sulfate heptahydrate ($FeSO_4{\cdot}7H_2O$, ≥99.0%), anhydrous sodium sulfate (Na_2SO_4, ≥99.5%), and sodium perchlorate monohydrate ($NaClO_4$, ≥99.0%) were purchased from Aladdin Industrial Corporation, without undergoing any additional purification processes. Ethylene carbonate (EC, 99.95%), dimethyl carbonate (DMC, 99.99%), ethyl methyl carbonate (EMC, 99.98%), and fluoroethylene carbonate (FEC, 99.9%) were bought from the DodoChem website. Electrically conductive carbon black plus (ECP, D_{50} = 34 nm), poly(vinylidene fluoride) (PVDF HSV900), Whatman GF/D glass fiber separator (average pores size of 2.7 μm), and Al foil (Al > 99.999%, 20 μm) were purchased from Canrd New Energy Technology Corporation.

4.2. Material Synthesis. The samples were prepared utilizing the thermal shock (TS) strategy. In concrete terms, a conductive substrate as a heating device, specifically a carbon cloth measuring 5.0 cm × 2.5 cm and sourced from Taiwan Carbon Energy Technology, was applied. The carbon cloth heater was powered by a direct current power supply (model MPS0100D) with a current range of 0−100 A and a voltage range of 0−50 V. The temperature of the heater was adjusted by manipulating the current and voltage and was measured using a laser infrared thermometer (manufactured by Sanya Kechuang Future Technology).

Benefiting from the acceleration of the reaction kinetics through TS treatment, the target material was successfully synthesized by a low-temperature solid-state method within a significantly shortened time with or without prior dehydrating $FeSO_4{\cdot}7H_2O$. Specifically, stoichiometric amounts of anhydrous Na_2SO_4, $FeSO_4{\cdot}7H_2O$, and conductive carbon were evenly mixed via a ball-milling process to obtain a mechanical preactivation mixture, followed by drying under vacuum at 60 °C for 12 h. The collected precursor was loaded onto a carbon cloth in an Ar atmosphere. After several thermal shocks, the product from the hydrous precursor was further pelletized and treated (denoted as HS-NFS) in a tube furnace at 350 °C for 6 h in an Ar flow at a ramp rate of 3 °C min^{-1}. In addition, anhydrous $FeSO_4$ was obtained by dehydrating $FeSO_4{\cdot}7H_2O$ by TS treatment in an Ar atmosphere. The target product (denoted as AS-NFS) from the anhydrous precursor was also prepared using the above process. For comparison, the two aforementioned precursors were pelletized and sintered at 350 °C for 24 h in an Ar atmosphere at a heating rate of 3 °C min^{-1} without additional TS treatment and were denoted as HF-NFS and AF-NFS, respectively.

4.3. Material Characterization. The samples were subjected to X-ray diffraction (XRD) analysis to determine their compositions and crystal structures, which was conducted by using a Bruker D8 Focus polycrystalline powder diffractometer. Scanning electron microscopy (SEM) images were acquired using a JSM-7800F instrument.

Transmission electron microscopy (TEM) and high-resolution transmission electron microscopy (HRTEM) images were obtained using a JEM-ARM200F instrument. Thermogravimetric analysis was conducted with a Mettler Toledo thermogravimetry scanning calorimeter (TGA/DSC) at heating rates of 3 and 100 °C min^{-1} from room temperature to 400 and 500 °C, respectively. The surface information of Fe was obtained using a Thermo Fisher (ESCALAB 250XI) instrument by X-ray photoelectron spectroscopy (XPS) analysis. The carbon content of the samples was measured by a carbon−sulfur analyzer (CS-902, Wanlianda Xinke, Beijing, China). Electrical resistivity was measured by a four-probe resistivity tester (ST2722-SZ, Jingge, Suzhou, China).

4.4. Electrochemical Measurement. ECP was selected as a conductive agent due to its unique branched chain with many conductive contact points and more conductive paths compared with super P, which can improve the dispersion of slurry and reduce the internal resistance of the battery. Working electrodes of 70 wt % active material, 20 wt % ECP, and 10 wt % poly(vinylidene fluoride) were mixed in *N*-methylpyrrolidone (NMP). Subsequently, the resulting slurry was uniformly cast onto carbon-coated aluminum foil with an average loading of ≈1.5 mg cm^{-2} and dried at 100 °C under vacuum. The electrolyte was prepared by dissolving 1 M $NaClO_4$ in a mixed solution of PC/DMC/EMC (1:1:1 by volume) with the addition of 5% (in volume) FEC. A GF/D glass fiber filter was utilized as the separator. 2032-type coin cells were assembled using the cathode film as the working electrode, while Na metal foils served as the counter and reference electrodes. The assembly process was performed inside an Ar-filled glovebox, where the concentrations of O_2 and H_2O were carefully controlled to below 0.1 ppm. For electrochemical characterization of the prepared electrodes, a Neware test system (Neware Technology Limited) was employed. Galvanostatic charge−discharge (GCD) cycling and rate capability tests were conducted within the voltage range of 2.0−4.3 V, at different rates ranging from C/10 to 20C (1C = 120 mAh g^{-1}). All tests were performed in a constant-temperature environment at 25 ± 1 °C. In addition, electrochemical impedance spectroscopy (EIS) was performed over a frequency range of 100 kHz to 10 mHz, with an amplitude of 10 mV (AC) by utilizing an electrochemical workstation (CHI 660E). Cyclic voltammetry (CV) tests were conducted at a scan speed of 0.1 mV s^{-1}. Furthermore, a galvanostatic intermittent titration technique (GITT) test was performed using a Neware battery testing system. The testing rate for GITT was set at 0.1C (12 mA g^{-1}), and the potential window was 2.0−4.3 V vs Na$^+$/Na. The duration time for each applied galvanostatic current and rest was 0.5 and 5 h, respectively.

■ ASSOCIATED CONTENT

Supporting Information

The Supporting Information is available free of charge at https://pubs.acs.org/doi/10.1021/acsami.3c19618.

> TGA-DSC profiles; XRD patterns; Rietveld refinement results based on XRD; XPS spectrum; SEM images; TEM images; CV curves; electrochemical performance of AS-NFS and AF-NFS electrodes (PDF)

■ AUTHOR INFORMATION

Corresponding Authors

Yanan Chen − *School of Materials Science and Engineering, Tianjin University, Tianjin 300072, P. R. China;* orcid.org/0000-0002-6346-6372; Email: yananchen@tju.edu.cn

Jia Ding − *School of Materials Science and Engineering, Tianjin University, Tianjin 300072, P. R. China;* orcid.org/0000-0001-7258-9430; Email: jiading@tju.edu.cn

Authors

Yuhang Liu − *School of Materials Science and Engineering, Tianjin University, Tianjin 300072, P. R. China*

Yujun Han − *School of Materials Science and Engineering, Tianjin University, Tianjin 300072, P. R. China*

Zijing Song − *School of Materials Science and Engineering, Tianjin University, Tianjin 300072, P. R. China*

Wanqing Song − *School of Materials Science and Engineering, Tianjin University, Tianjin 300072, P. R. China*

Zhikai Miao − *School of Materials Science and Engineering, Tianjin University, Tianjin 300072, P. R. China*

Wenbin Hu − *School of Materials Science and Engineering, Tianjin University, Tianjin 300072, P. R. China*

Complete contact information is available at: https://pubs.acs.org/10.1021/acsami.3c19618

Notes

The authors declare no competing financial interest.

■ ACKNOWLEDGMENTS

This work was financially supported from the National Natural Science Foundation of China (52072257, 52372218)

■ REFERENCES

(1) Yabuuchi, N.; Kubota, K.; Dahbi, M.; Komaba, S. Research Development on Sodium-Ion Batteries. *Chem. Rev.* **2014**, *114* (23), 11636−11682.

(2) Lin, J.; Ding, J.; Wang, H.; Yang, X.; Zheng, X.; Huang, Z.; Song, W.; Ding, J.; Han, X.; Hu, W. Boosting Energy Efficiency and Stability of Li−CO_2 Batteries via Synergy between Ru Atom Clusters and Single-Atom Ru−N_4 sites in the Electrocatalyst Cathode. *Adv. Mater.* **2022**, *34* (17), No. 2200559.

(3) Wang, X.; Ding, J.; Song, W.; Yang, X.; Zhang, T.; Huang, Z.; Wang, H.; Han, X.; Hu, W. Cation Vacancy Clusters in $Ti_3C_2T_x$ MXene Induce Ultra-Strong Interaction with Noble Metal Clusters for Efficient Electrocatalytic Hydrogen Evolution. *Adv. Energy Mater.* **2023**, *13* (23), No. 2300148.

(4) Song, W.; Xiao, C.; Ding, J.; Huang, Z.; Yang, X.; Zhang, T.; Mitlin, D.; Hu, W. Review of Carbon Support Coordination Environments for Single Metal Atom Electrocatalysts (SACS). *Adv. Mater.* **2024**, *36* (1), No. 2301477.

(5) Islam, M. S.; Fisher, C. A. J. Lithium and sodium battery cathode materials: computational insights into voltage, diffusion and nanostructural properties. *Chem. Soc. Rev.* **2014**, *43* (1), 185−204.

(6) Zhao, C.; Wang, Q.; Yao, Z.; Wang, J.; Sánchez-Lengeling, B.; Ding, F.; Qi, X.; Lu, Y.; Bai, X.; Li, B.; et al. Rational design of layered oxide materials for sodium-ion batteries. *Science* **2020**, *370* (6517), 708−711.

(7) Huang, Z.; Li, H.; Yang, Z.; Wang, H.; Ding, J.; Xu, L.; Tian, Y.; Mitlin, D.; Ding, J.; Hu, W. Nanosecond laser lithography enables concave-convex zinc metal battery anodes with ultrahigh areal capacity. *Energy Storage Mater.* **2022**, *51*, 273−285.

(8) Barpanda, P. Pursuit of Sustainable Iron-Based Sodium Battery Cathodes: Two Case Studies. *Chem. Mater.* **2016**, *28* (4), 1006−1011.

(9) Nayak, P. K.; Yang, L.; Brehm, W.; Adelhelm, P. From Lithium-Ion to Sodium-Ion Batteries: Advantages, Challenges, and Surprises. *Angew. Chem., Int. Ed.* **2018**, *57* (1), 102−120.

(10) Guo, J.; Feng, F.; Zhao, S.; Shi, Z.; Wang, R.; Yang, M.; Chen, F.; Chen, S.; Ma, Z.-F.; Liu, T. High FeLS(C) electrochemical activity of an iron hexacyanoferrate cathode boosts superior sodium ion storage. *Carbon Energy* **2023**, *5* (5), No. e314.

(11) Chen, T.; Ouyang, B.; Fan, X.; Zhou, W.; Liu, W.; Liu, K. Oxide cathodes for sodium-ion batteries: Designs, challenges, and perspectives. *Carbon Energy* **2022**, *4* (2), 170−199.

(12) Li, Y.; Zhou, Q.; Weng, S.; Ding, F.; Qi, X.; Lu, J.; Li, Y.; Zhang, X.; Rong, X.; Lu, Y.; et al. Interfacial engineering to achieve an

energy density of over 200 Wh kg−1 in sodium batteries. *Nat. Energy* **2022**, *7* (6), 511−519.

(13) Kundu, D.; Talaie, E.; Duffort, V.; Nazar, L. F. The Emerging Chemistry of Sodium Ion Batteries for Electrochemical Energy Storage. *Angew. Chem., Int. Ed.* **2015**, *54* (11), 3431−3448.

(14) Xu, M.; Liu, M.; Yang, Z.; Wu, C.; Qian, J. Research Progress on Presodiation Strategies for High Energy Sodium-Ion Batteries. *Acta Phys. -Chim. Sin.* **2023**, *39* (3), No. 2210043, DOI: 10.3866/pku.whxb202210043.

(15) Dai, Z.; Mani, U.; Tan, H. T.; Yan, Q. Advanced Cathode Materials for Sodium-Ion Batteries: What Determines Our Choices? *Small Methods* **2017**, *1* (5), No. 1700098.

(16) Palomares, V.; Serras, P.; Villaluenga, I.; Hueso, K. B.; Carretero-González, J.; Rojo, T. Na-ion batteries, recent advances and present challenges to become low cost energy storage systems. *Energy Environ. Sci.* **2012**, *5* (3), 5884−5901.

(17) Song, Z.; Liu, R.; Liu, W.; Chen, Y.; Hu, W. Low-Cost Polyanion-Type Cathode Materials for Sodium-Ion Battery. *Adv. Energy Sustainability Res.* **2023**, *4* (11), No. 2300102.

(18) Fu, H.; Wang, Y.-P.; Fan, G.; Guo, S.; Xie, X.; Cao, X.; Lu, B.; Long, M.; Zhou, J.; Liang, S. Synergetic stability enhancement with magnesium and calcium ion substitution for Ni/Mn-based P2-type sodium-ion battery cathodes. *Chem. Sci.* **2022**, *13* (3), 726−736.

(19) Jin, T.; Li, H.; Zhu, K.; Wang, P. F.; Liu, P.; Jiao, L. Polyanion-type cathode materials for sodium-ion batteries. *Chem. Soc. Rev.* **2020**, *49* (8), 2342−2377.

(20) Gutierrez, A.; Benedek, N. A.; Manthiram, A. Crystal-Chemical Guide for Understanding Redox Energy Variations of $M^{2+/3+}$ Couples in Polyanion Cathodes for Lithium-Ion Batteries. *Chem. Mater.* **2013**, *25* (20), 4010−4016.

(21) Barpanda, P.; Oyama, G.; Nishimura, S.; Chung, S. C.; Yamada, A. A 3.8-V earth-abundant sodium battery electrode. *Nat. Commun.* **2014**, *5*, No. 4358.

(22) Chen, M.; Cortie, D.; Hu, Z.; Jin, H.; Wang, S.; Gu, Q.; Hua, W.; Wang, E.; Lai, W.; Chen, L.; et al. A Novel Graphene Oxide Wrapped $Na_2Fe_2(SO_4)_3$/C Cathode Composite for Long Life and High Energy Density Sodium-Ion Batteries. *Adv. Energy Mater.* **2018**, *8* (27), No. 1800944, DOI: 10.1002/aenm.201800944.

(23) Zhang, J.; Yan, Y.; Wang, X.; Cui, Y.; Zhang, Z.; Wang, S.; Xie, Z.; Yan, P.; Chen, W. Bridging multiscale interfaces for developing ionically conductive high-voltage iron sulfate-containing sodium-based battery positive electrodes. *Nat. Commun.* **2023**, *14* (1), No. 3701.

(24) Oyama, G.; Nishimura, S.-i.; Suzuki, Y.; Okubo, M.; Yamada, A. Off-Stoichiometry in Alluaudite-Type Sodium Iron Sulfate $Na_{2+2x}Fe_{2-x}(SO_4)_3$ as an Advanced Sodium Battery Cathode Material. *ChemElectroChem* **2015**, *2* (7), 1019−1023.

(25) Watcharatharapong, T.; Chakraborty, S.; Ahuja, R. Defect Thermodynamics in Nonstoichiometric Alluaudite-Based Polyanionic Materials for Na-Ion Batteries. *ACS Appl. Mater. Interfaces* **2019**, *11* (36), 32856−32868.

(26) Plewa, A.; Kulka, A.; Hanc, E.; Zając, W.; Sun, J.; Lu, L.; Molenda, J. Facile aqueous synthesis of high performance $Na_2FeM(SO_4)_3$ (M = Fe, Mn, Ni) alluaudites for low cost Na-ion batteries. *J. Mater. Chem. A* **2020**, *8* (5), 2728−2740.

(27) Barman, P.; Dwibedi, D.; Jayanthi, K.; Meena, S. S.; Nagendran, S.; Navrotsky, A.; Barpanda, P. Aqueous spray-drying synthesis of alluaudite $Na_{2+2x}Fe_{2-x}(SO_4)_3$ sodium insertion material: studies of electrochemical activity, thermodynamic stability, and humidity-induced phase transition. *J. Solid State Electrochem.* **2022**, *26* (9), 1941−1950.

(28) Dwibedi, D.; Barpanda, P. Sodium Metal Sulphate Alluaudite Class of High Voltage Battery Insertion Materials. *MRS Adv.* **2018**, *3* (22), 1209−1214.

(29) Fang, Y.; Liu, Q.; Feng, X.; Chen, W.; Ai, X.; Wang, L.; Wang, L.; Ma, Z.; Ren, Y.; Yang, H.; Cao, Y. An advanced low-cost cathode composed of graphene-coated $Na_{2.4}Fe_{1.8}(SO_4)_3$ nanograins in a 3D graphene network for ultra-stable sodium storage. *J. Energy Chem.* **2021**, *54*, 564−570.

(30) Dwibedi, D.; Ling, C. D.; Araujo, R. B.; Chakraborty, S.; Duraisamy, S.; Munichandraiah, N.; Ahuja, R.; Barpanda, P. Ionothermal Synthesis of High-Voltage Alluaudite $Na_{2+2x}Fe_{2-x}(SO_4)_3$ Sodium Insertion Compound: Structural, Electronic, and Magnetic Insights. *ACS Appl. Mater. Interfaces* **2016**, *8* (11), 6982−6991.

(31) Di, H.; Yue, H.; Qi, H.; Zhang, D.; Chen, G. $Na_{2+2x}Fe_{2-x}(SO_4)_3$@rice husks carbon composite as a high-performance cathode material for sodium-ion batteries. *Ionics* **2019**, *25* (8), 3727−3736.

(32) Zhu, W.; Zhang, J.; Luo, J.; Zeng, C.; Su, H.; Zhang, J.; Liu, R.; Hu, E.; Liu, Y.; Liu, W. D.; et al. Ultra-fast non-equilibrium synthesis of cathode materials for Li-ion batteries. *Adv. Mater.* **2022**, No. e2208974, DOI: 10.1002/adma.202208974.

(33) Guo, Z.; Jiang, H.; Sun, X.; Li, X.; Liu, Z.; Zhang, J.; Luo, J.; Zhang, J.; Tao, X. S.; Ding, J.; et al. Ultrafast Non-Equilibrium Phase Transition Induced Twin Boundaries of Spinel Lithium Manganate. *Adv. Energy Mater.* **2024**, *14* (5), No. 2302484.

(34) Shishkin, M.; Sato, H. Ab Initio Study of Stability of $Na_2Fe_2(SO_4)_3$, a High Potential Na-Ion Battery Cathode Material. *J. Phys. Chem. C* **2017**, *121* (37), 20067−20074.

(35) Sauer, B. B.; Kampert, W. G.; Neal Blanchard, E.; Threefoot, S. A.; Hsiao, B. S. Temperature modulated DSC studies of melting and recrystallization in polymers exhibiting multiple endotherms. *Polymer* **2000**, *41* (3), 1099−1108.

(36) Reynaud, M.; Rousse, G.; Abakumov, A. M.; Sougrati, M. T.; Van Tendeloo, G.; Chotard, J.-N.; Tarascon, J.-M. Design of new electrode materials for Li-ion and Na-ion batteries from the bloedite mineral $Na_2Mg(SO_4)_2 \cdot 4H_2O$. *J. Mater. Chem. A* **2014**, *2* (8), 2671−2680.

(37) Jungers, T.; Mahmoud, A.; Malherbe, C.; Boschini, F.; Vertruyen, B. Sodium iron sulfate alluaudite solid solution for Na-ion batteries: moving towards stoichiometric $Na_2Fe_2(SO_4)_3$. *J. Mater. Chem. A* **2019**, *7* (14), 8226−8233.

(38) Meng, Y.; Yu, T.; Zhang, S.; Deng, C. Top-down synthesis of muscle-inspired alluaudite $Na_{2+2x}Fe_{2-x}(SO_4)_3$/SWNT spindle as a high-rate and high-potential cathode for sodium-ion batteries. *J. Mater. Chem. A* **2016**, *4* (5), 1624−1631.

(39) Liu, X.; Tang, L.; Xu, Q.; Liu, H.; Wang, Y. Ultrafast and ultrastable high voltage cathode of $Na_{2+2x}Fe_{2-x}(SO_4)_3$ microsphere scaffolded by graphene for sodium ion batteries. *Electrochim. Acta* **2019**, *296*, 345−354.

(40) Ji, G.; Wang, J.; Liang, Z.; Jia, K.; Ma, J.; Zhuang, Z.; Zhou, G.; Cheng, H.-M. Direct regeneration of degraded lithium-ion battery cathodes with a multifunctional organic lithium salt. *Nat. Commun.* **2023**, *14* (1), No. 584.

(41) Goñi, A.; Iturrondobeitia, A.; de Muro, I. G.; Lezama, L.; Rojo, T. $Na_{2.5}Fe_{1.75}(SO_4)_3$/Ketjen/rGO: An advanced cathode composite for sodium ion batteries. *J. Power Sources* **2017**, *369*, 95−102.

(42) Liu, Y.; Rajagopalan, R.; Wang, E.; Chen, M.; Hua, W.; Zhong, B.; Zhong, Y.; Wu, Z.; Guo, X. Insight into the Multirole of Graphene in Preparation of High Performance $Na_{2+2x}Fe_{2-x}(SO_4)_3$ Cathodes. *ACS. Susutainable Chem. Eng.* **2018**, *6* (12), 16105−16112.

(43) Zhang, M.; Qi, H.; Qiu, H.; Zhang, T.; Zhao, X.; Yue, H.; Chen, G.; Wang, C.; Wei, Y.; Zhang, D. Reduced graphene oxide wrapped alluaudite $Na_{2+2x}Fe_{2-x}(SO_4)_3$ with high rate sodium ion storage properties. *J. Alloys Compd.* **2018**, *752*, 267−273.

(44) Yu, T.; Lin, B.; Li, Q.; Wang, X.; Qu, W.; Zhang, S.; Deng, C. First exploration of freestanding and flexible $Na_{2+2x}Fe_{2-x}(SO_4)_3$@porous carbon nanofiber hybrid films with superior sodium intercalation for sodium ion batteries. *Phys. Chem. Chem. Phys.* **2016**, *18* (38), 26933−26941.

(45) Dwibedi, D.; Araujo, R. B.; Chakraborty, S.; Shanbogh, P. P.; Sundaram, N. G.; Ahuja, R.; Barpanda, P. $Na_{2.44}Mn_{1.79}(SO_4)_3$: a new member of the alluaudite family of insertion compounds for sodium ion batteries. *J. Mater. Chem. A* **2015**, *3* (36), 18564−18571.

(46) Oyama, G.; Pecher, O.; Griffith, K. J.; Nishimura, S.-i.; Pigliapochi, R.; Grey, C. P.; Yamada, A. Sodium Intercalation Mechanism of 3.8 V Class Alluaudite Sodium Iron Sulfate. *Chem. Mater.* **2016**, *28* (15), 5321−5328.

(47) Wang, W.; Liu, X.; Xu, Q.; Liu, H.; Wang, Y.-G.; Xia, Y.; Cao, Y.; Ai, X. A high voltage cathode of $Na_{2+2x}Fe_{2-x}(SO_4)_3$ intensively protected by nitrogen-doped graphene with improved electrochemical performance of sodium storage. *J. Mater. Chem. A* **2018**, *6* (10), 4354−4364.

(48) Wong, L. L.; Chen, H. M.; Adams, S. Sodium-ion diffusion mechanisms in the low cost high voltage cathode material $Na_{2+\delta}Fe_{2-\delta/2}(SO_4)_3$. *Phys. Chem. Chem. Phys.* **2015**, *17* (14), 9186−9193.

(49) Zheng, W.; Shui, M.; Shu, J.; Gao, S.; Xu, D.; Chen, L.; Feng, L.; Ren, Y. GITT studies on oxide cathode $LiNi_{1/3}Co_{1/3}Mn_{1/3}O_2$ synthesized by citric acid assisted high-energy ball milling. *Bull. Mater. Sci.* **2013**, *36* (3), 495−498.

(50) Sun, S.; Chen, Y.; Bai, Q.; Huang, Q.; Liu, C.; He, S.; Yang, Y.; Wang, Y.; Guo, L. Unraveling the modified regulation of ternary substitution on $Na_3V_2(PO_4)_3$ for sodium ion batteries. *J. Mater. Chem. A* **2022**, *10* (21), 11340−11353.

(51) Jiang, H.; Qian, G.; Liu, R.; Liu, W.-D.; Chen, Y.; Hu, W. Effects of elemental doping on phase transitions of manganese-based layered oxides for sodium-ion batteries. *Sci. China Mater.* **2023**, *66* (12), 4542−4549.